Published in final edited form as:
Nat Photonics. 2021 October ; 15(10): 738–742. doi:10.1038/s41566-021-00878-9.

Solution-processed PbS quantum dot infrared laser with room-temperature tuneable emission in the optical telecommunications window

G. L. Whitworth[1], **M. Dalmases**[1], **N. Taghipour**[1], **G. Konstantatos**[1,2,*]

[1]ICFO, Institut de Ciencies Fotoniques, The Barcelona Institute of Science and Technology, Castelldefels (Barcelona) 08860Spain

[2]ICREA, Institució Catalana de Recerca i Estudis Avançats, 08010 Barcelona, Spain

Abstract

Solution processed semiconductor lasers have achieved much success across the nanomaterial research community, including in organic semiconductors[1,2], perovskites[3,4] and colloidal semiconductor nanocrystals[5,6]. The ease of integration with other photonic components, and the potential for upscaling using emerging large area fabrication technologies, such as roll-to-roll[7], make these lasers attractive as low-cost photonic light sources that can find use in a variety of applications: integrated photonic circuitry[8,9], telecommunications[10,11], chemo-/bio-sensing[12,13], security[14], and lab-on-chip experiments[15]. However, for fiber-optic or free-space optical (FPO) communications and eye-safe LIDAR applications, room temperature solution-processed lasers have remained elusive. Here we report the first solution processed laser, comprising PbS colloidal quantum dots (CQDs) integrated on a distributed feedback (DFB) cavitiy, with tuneable lasing wavelength from 1.55 μm – 1.65 μm. These lasers operate at room temperature and exhibit linewidths as low as ~0.9 meV.

Owing to their wavelength tunability, high quantum confinement potential and solution processability, colloidal quantum dots have been employed successfully to a wide variety of optoelectronic devices, such as LEDs[16], photovoltaics[17,18], lasers[19–22] and photodetectors[22,23]. However, demonstrations of optical gain and lasing have largely been confined to CdSe-based visible emitters due to their high gain and low degeneracy[6,20–22,24,25]. The 8-fold degeneracy of PbS(e) CQDs has limited the gain performance of Pb-salt semiconductor nanocrystals along with high temperature dependant Auger recombination rates[21,26]. In view of this, and despite optical gain in PbS(e) being demonstrated as early as 2003[27], room-temperature lasing has yet to be reported. Only one

---

[*] Gerasimos.konstantatos@icfo.eu .

Author Contributions
G.K. designed supervised and directed the study. G.W. designed the experiments, performed the theoretical modelling, fabricated and characterized the laser structures and the thin films. M.D. sythesised the quantum dot materials. N.T. contributed to thin film and laser development. G.W. and G.K. wrote the manuscript with inputs from the co-authors.

Competing interests
The authors declare no competing interest

report of cryogenic CQD PbS lasing has been made where a CQD filled microcapillary to generate a whispering gallery mode laser with a FWHM of 11 nm[28]. This was performed at cryogenic temperatures to inhibit Auger recombination but room temperature lasing could not be observed. Recently lasing at 1374 nm was reported by Ag_2Se CQDs in a micro-ring “coffee stain” resonator, however this is neither practical nor can be easily tuned[29]. While CQD lasing employing industrially relevant optical cavities has been extensively reported in the visible[20–22], it has remained elusive for the infrared. Herein, we employ a DFB cavity on a highly thermally conductive substrate to achieve the first infrared CQD room-temperature, eye-safe lasing, tuneable across the minimum-loss window of the telecommunications spectrum (known as the central, C-, and long-wavelength, L- bands). Additionally we go on to demonstrate a 40% reduction in lasing threshold by employing a heavily n-doped PbS CQD film[30].

Due to their low thresholds, high modal selectivity, and solution processing compatibility, a distributed feedback architecture was chosen as the ideal, industrially relevant photonic cavity to achieve lasing in PbS CQDs[20–22]. DFB lasers are waveguide gain structures whereby a periodic modulation in the effective refractive index, n_{eff}, gives arise to a photonic bandgap and therefore high band-edge reflectivity to form an optical cavity when the Bragg condition is satisfied[31,32]:

$$m\lambda_B = 2n_{eff}\Lambda \tag{1}$$

where λ_B is the feedback lasing wavelength, Λ is the period of modulation, and m is the order of diffraction used to generate optical feedback. All lasers presented were designed as 1D second-order DFB lasers ($m = 2$). The periodic modulation in the waveguide is typically made by fabricating a nanostructured grating substrate and depositing the desired thickness of gain material (CQDs) in order to satisfy equation(1) at the desired wavelength. Gratings were fabricated out of sapphire (Al_2O_3) substrates using e-beam lithography and subsequent reactive ion etching pattern transfer as schematically shown in Fig. 1a. Sapphire was chosen for its high thermal conductivity to avoid excessive heating in the CQDs when optically pumped, which would cause a blue-shifting gain spectrum and exacerbate Auger recombination losses (Supplementary Information section I). CQDs were spin-coated on gratings followed by a subsequent ligand exchange in a layer-by-layer fashion as described in Methods to achieve a desired thickness (Fig. 1a).

To precisely design the DFB cavity to achieve lasing at the amplified spontaneous emission (ASE) peak of the PbS CQDs, a variable gain finite-difference frequency domain (FDFD) model was used in order to mimic experimental reality and predict exact DFB lasing cavity modes[31,32] (Supplementary Information section II). The refractive index and extinction coefficient of films made of 5.7 nm quantum dots, (absorption peak @ 1520 nm) was measured via ellipsometry (Fig. 1b.) and input into an in-house built FDFD solver. Gain was introduced into the simulation by subtracting a Gaussian of variable amplitude, A_g, from the extinction coefficient, plotted in Fig. 1b, the parameters of which match the measured ASE profile of the unstructured CQD film (peak wavelength, $\lambda_{ASE} = 1600\ nm$, and standard deviation, σ_{ASE} such that:

$$\tilde{n}_\lambda = n_\lambda + i\left\{k_\lambda - A_g e^{-(\lambda - \lambda_{ASE})^2}/2\sigma_{ASE}^2\right\} \tag{2}$$

where $\tilde{n}_\lambda$ is the complex refractive index and n_λ and k_λ are the ellipsometry measured refractive index and extinction coefficient respectively. Fig. 1c,d show the resultant transverse electric (TE) E_z-field at 1600 nm, for a DFB structure at zero gain, $A_g = 0$, and at cavity gain, $A_g = 0.103$. As can be seen in Fig. 1e, at the cavity gain, optical confinement is significantly increased, with a field enhancement factor nearly 4 orders of magnitude higher than that of zero gain. Fig. 1f shows the simulated transmission spectrum of the structure at cavity gain, depicting a peak above unity transmission, centred at the desired lasing wavelength of 1600 nm. The schematic representation of the fabrication process shown in Fig. 1a was then followed to create the desired simulated structure, a cross-sectional image of which can be seen in Fig. 1g. From this this image we measure the grating height to be 49 ± 5 nm and the CQD layer thickness above this to be 107 ± 5 nm (see Methods and Supplementary Information section III). The average width of the grating ridges was measured to be ~ 305 ± 10 nm yielding a duty cycle of 0.34 with a sidewall angle of 20° (see Supplementary Information section II).

The transmission spectrum of the fabricated DFB was measured using an FTIR spectrometer and compared to the simulated structure at zero gain (Fig. 2a). In both spectra, the exciton absorption dip can be clearly seen at 1520 nm along with an additional diffraction dip (arrows) positioned around 1600 nm, indicating good agreement between experiment and simulations. From this transmission resonance, the Q-factor was extracted to be 89. This relatively low value has been indentified to be due to the high ground state self absorption of the CQDs and because of the high refractive index contrast between the CQDs and the sapphire substrate as discussed in Supplementary Information section XI. The sample was then optically pumped using a femtosecond Yt:YAG 1030 nm laser and the DFB laser emission was collected perpendicular to the surface as described in Methods (Fig. 2b). Fig. 2c shows the collected spectrum below (black) and above (red) lasing threshold along with the ASE profile (blue). Above threshold the FWHM of the spectra drops dramatically to 3 nm (~ 1.5 meV), shown in Fig. 2d. Insets show the surface of the CQD DFB above and below threshold. Below threshold the pump stripe can be seen overlapping with a central 1 mm x 1 mm grating, along with adjacent gratings present on the sample; above threshold, intense light emission is emitted from the grating area (Supplementary Video 1). The integrated spectral output is plotted against the optical pump fluence in Fig. 2e, measuring the pump fluence lasing threshold to be 930 μJ/cm^2 along with an inset above-threshold beam profile. Assuming a packing density of 74% the CQDs in the film and with a measured absorption of 8.7 % at 1030 nm, this pump fluence equates to an average exciton population per dot of $\langle N \rangle = 4.3$, in good agreement with previously reported thresholds for optical gain and stimulated emission from this system[30].

By varying the DFB grating period by 5 nm, tuneable lasing was achieved across the telecommunications L-band (1565 nm – 1625 nm) using the same quantum dot films (Diameter = 5.7 nm), lasing from 1588 nm – 1600 nm. To expand the lasing across to the adjacent central C-band (1530 nm - 1565 nm) and the ultra-long U-band (1625 nm –

1675 nm), 5.4 nm and 6.0 nm CQDs were synthesised with corresponding ASE peaks at 1558 nm and 1648 nm respectively. Using the previously described steps of simulations and fabrication, fully tuneable lasing was achieved, traversing the telecommunications minimum-loss window, from 1553 nm – 1649 nm, as shown in Fig. 3a. The inset is a box-chart of the FWHM of the measured laser spectra with an average of 1.7 ± 0.5 meV (3.4 ± 1 nm) with some exhibiting single-mode behaviour with linewidth as narrow as 0.9 meV (< 2nm) at 1629 nm. Whilst these linewidth energies compare well to other experimental infrared semiconductor DFB lasers[33,34] (see Supplementary Information section IV), they remain broad when compared to off-the-shelf, industrial grade DFB lasers, due to their low Q-factors as discussed in Supplementary Information section XI. Additionally, it has been reported previously that high carrier density transients generated from pulsed excitation arises the wavelength chirp effect and therefore linewidth broadening[33].

Fig. 3b plots the measured thresholds of the individual lasers presented in Fig. 3a along with the ASE threshold of the respective quantum dots. We can see in the case of the L-band lasing, lasing thresholds were lower than that of unstructured film ASE threshold, indicating a high degree of optical confinement improving the radiative emission of the quantum dots in the cavity. Also observed is that for lasing which was blue shifted compared to that of the ASE peak, as in the case of the C-band lasers, the threshold rapidly increased from that of the ASE, indicating a rapid fall off in gain, despite the lower self-absorption losses. Additional lasing stability and polarisation measurments can be found in Supplementary Information section V. Polarisation measurments confirmed these lasers to be operating on the TE mode.

With the successful demonstration of tuneable lasing from intrinsic PbS quantum dots, we go on to demonstrate lasing in robustly n-doped PbS quantum dots. Using 1-Ethyl-3-methylimidazolium iodide (EMII) inside the ligand exchange solution, I^- anions are exchanged with exposed S^{2-} ions on the exposed (100) crystal plane surface of the quantum dots as shown in Fig. 4a. Doping is achieved following a subsequent alumina atomic layer deposition (ALD), where atmospheric electron acceptors (water/oxygen) are removed from theCQD surface, simultaneously encapsulating the film (as described in previous work[30]). This anionic exchange populates the conduction band of the CQD with electrons, reducing the number of excitons per dot needed to achieve population inversion[24, 30]. Whilst doping electrons in the conduction band lead to higher Auger losses for single excitons, the reduction in gain threshold results in an overall reduction of Auger recombination at threshold when comparing doped and undoped CQDs[30]. The FTIR transmission spectra of undoped and doped CQDs can be seen in Fig. 4b. A clear bleaching of the exciton peak is observed, corresponding to a CB occupancy of $\langle N \rangle = 3.2$.

Following the same process as previously described, a doped CQD laser at 1650 nm was fabricated; the input/output characteristic of which is shown in Fig. 4c. The doped lasing threshold was measured to be 430 μJ/cm^2 of optical pump fluence. This represents a 43 % reduction in lasing threshold compared to an undoped CQD laser of the same wavelength which was measured to be 770 μJ/cm^2. This matches well to the ~ 40 % occupancy of the conduction band as measured by the FTIR transmission (see Methods) supporting a threshold reduction due to the n-doping of the CQDs[30]. The doped sample was additionally tested under higher energy pumping conditions by using the 515 nm, frequency doubled output of the Yt:YAG laser. Under green pumping, thresholds increased by a factor of 1.4 due to higher multi-excitonic interactions, in agreement with previous reports[35,36] (Supplementary Information section VI).

In conclusion, we have presented the very first room-temperature tuneable infrared CQD lasers. This was achieved by using PbS quantum dots which in themselves can be tuned to provide gain across the entire minimum-loss region (C- and L- bands) of the telecommunications windows. Combining these CQDs with highly thermally conductive gratings, DFB lasers were fabricated, creating lasing from 1553 nm to 1649 nm with an average FWHM of 1.7 ± 0.5 meV; going down to values as low as 0.9 meV. The design of the lasers was facilitated by an in-house built variable gain FDFD solver to accurately predict lasing spectra. Following this we demonstrated a 40% lasing threshold reduction via an anionic exchange during CQD deposition to n-dope the PbS CQDs. These results demonstrate that the previously considered limitations of PbS quantum dots such as high degeneracy and high room-temperature Auger recombination rates can all be overcome. With further photonic and material improvements these infrared, solution-processed Pb-chalcogenide DFB lasers have great potential in integrated photonics, operating at wavelengths ideal for fibre optic and eye-safe FSO telecommunication and LIDAR applications.

Methods

CQD Synthesis

PbS CQDs were synthesized under inert atmosphere by the hot injection method. A mixture of 0.446 g Lead (II) oxide (PbO), 50mL 1-Octadecene (ODE) and 3.8 mL of oleic acid were heated at 100°C under vacuum for 1h to form the lead precursor (lead oleate). Once under argon, a solution of hexamethyldisilathiane (HMS) in 3 mL ODE was quickly injected. After 6 minutes of reaction, a second solution of HMS in 9 mL of ODE was injected dropwise. Subsequently, the solution was cooled down naturally to room temperature. PbS CQDs were precipitated with the addition of a mixture of acetone/ethanol and redispersed in anhydrous toluene. This purification process was repeated two more times. Finally, the concentration of PbS CQDs was adjusted to 30mg/mL and the solution was bubbled with N_2 to avoid oxidation. The nanocrystal size was tuned by varying the amount of HMS used in each solution. PbO, oleic acid, and HMS were purchased from Sigma Aldrich. ODE was purchased from Alfa Aesar. Acetone, ethanol and anhydrous toluene were purchased from Scharlab. All reagents and solvents were used as received. CQD diameters were calculated using an empirical quadratic formula[37].

Grating Fabrication and Characterisation

Gratings were fabricated in a cleanroom by spin-coating PMMA (AR-P 662.04 Allresist GmbH) at 4000 rpm for 60 s on top of sapphire substrates (Ossila Ltd.) followed by a 2 min baking step at 150 °C. A conductive polymer layer (AR-PC 5090.02 Allresist GmbH) was then spin-coated on top at 2000 rpm and then baked at 90 °C. Samples were transferred to an electron beam lithography system (Crestec CABL 9000C). Afterward lithography, the conductive polymer layer was dissolved off in water for 60 s and the e-beam resist was developed for 2 min. Post development, reactive ion-etching was performed using 80 sccm of Ar and 20 sccm of CHF_3 under an RF power of 290 V for 5 minutes. The residual PMMA was then removed using an oxygen plasma asher followed by acetone/isopropanol cleaning. Focussed ion beam (FIB) milling was performed using a Zeiss Auriga and a 100 nm of gold layer was deposited on the DFB sample using a thermal evaporator (Nano 36 Kurt J. Lesker) at a base pressure of 10^{-6} mbar.

CQD deposition

Quantum dots were deposited on alumina gratings using the following steps; (i) A 30mg/ml solution of CQDs was spun at 2500 rpm on gratings for 30 seconds; (ii) A ligand exchange solution of 7mg/ml EMII in methanol + 0.01 % MPA was applied to the surface for 30 s; (iii) Samples were spun at 2500 rpm for 60 s while methanol was drop cast onto the surface in order to clean the substrate of unwanted ligands; (iv) steps (i)-(iii) were then repeated until the desired thickness of CQDs was reached. For doping the samples were subsequently transferred to an ALD machine for 30 cycles of alumina deposition.

Optical Characterisation

FTIR spectra were obtained using a Niolet iS50R FT-IT spectrometer. Conduction band occupancy, $\langle N \rangle$, was calculated by taking the ratio of exciton absorption area before and after doping. Ellipsometry was performed using a SOPRA GES-5E spectroscopic ellipsometer and the CQDs were modelled using a Tauc-Lorentz model with additional Gaussian oscillators for the primary exciton transition and additional higher energy transitions.

ASE and Lasing Characterisation

Samples were optically pumped using a 1030 nm, femtosecond Yt:YAG ORAGAMI laser (NKT Photonics) at a repetition rate of 50 kHz. Pulses were 300 fs long and were focussed down onto the samples using a cylindrical lens to a stripe of ~ 1.2 mm x 0.2 mm. ASE spectra were collected from the side of sample using a f = 50 mm, 2” lens and free-space coupled into a Kymera 328i spectrograph (Oxford Instruments. Andor) via a f = 200 mm lens through a 100 μm slit. Additional gain and loss measurements were taken from unstructured PbS CQD films (see Supplementary Information section VII).

Lasing spectra were collected perpendicular the surface ~20 cm away from DFB grating surface using a fibre coupled port of the spectrometer using a 10 μm slit to obtain high resolution. All ASE and lasing spectra use collected using a 1 s integration time except for the low-resolution below-threshold spectra which used 5 s. Experimental configurations for both ASE and lasing can be found in Supplementary Information section VIII. Beam profiles were taken using a NIT-WiDy-SenS-320V-ST InGaAs camera (Iberoptics Sistemas Ópticos), ~ 20 cm away from the sample surface. For imaging sample surfaces, a SWIR lens was attached to the camera. A long pass filter was used in all situations to block pump laser light. Spectral data and threshold calculations for all lasers presented can be found in Supplementary Information section IX.

FDFD Simulations

A two-dimensional FDFD electromagnetic solver code was written in MATLAB. Periodic boundaries were applied in the x-direction and PMLs were used in the y-direction. The width of the simulation was set equal to the period of the grating with the y direction equal to the height of the target structure plus a full wavelength above and below. The code was run iteratively over structural parameters (e.g. height and period), wavelength and gain amplitude, with the refractive index being adjusted accordingly for each iteration. Refractive indices for alumina was obtained from refractiveindex.info. Field enhancement factor (*FEF*) was calculated along the central axis according to the following equation:

$$FEF = \frac{\int |E_z|^2 dy}{\int |E_{source}|^2 dy} \tag{3}$$

where E_z denotes the resultant out-of-plane electric field from the FDFD simulations and E_{source} is the source field.

Supplementary Material

Refer to Web version on PubMed Central for supplementary material.

Acknowledgements

The authors acknowledge financial support from the European Research Council (ERC) under the European Union's Horizon 2020 research and innovation programme (grant agreement no. 725165, G.K.) and the Ministerio de Ciencia e Innovacion under grant agreement PID2020-112591RB-I00, G.K.. This project has received funding from the European Union's Horizon 2020 research and innovation programme under the Marie Skłodowska-Curie grant agreement No. 754558, N.T.. Additionally, this project has received funding from the Spanish State Research Agency, through the "Severo Ochoa" Center of Excellence CEX2019-000910-S, the CERCA Programme / Generalitat de Catalunya and Fundació Mir-Puig.

Data Availability

The data presented in this study are available in Zenodo with the identifier, 10.5281/zenodo.5112914. Supplementary information data are avialbale from the corresponding author upon reasonable request.

Code availability

FDFD MATLAB codes are available in Zenodo with the identifier, 10.5281/zenodo.5112914.

References

1. Samuel IDW, Turnbull GA. Organic semiconductor lasers. Chem Rev. 2007; 107 :1272–1295. [PubMed: 17385928]
2. Chénais S, Forget S. Recent advances in solid-state organic lasers. Polymer International. 2012; 61 :390–406.
3. Sutherland BR, Sargent EH. Perovskite photonic sources. Nat Photonics. 2016; 10 :295–302.
4. Qin C, et al. Stable room-temperature continuous-wave lasing in quasi-2D perovskite films. Nature. 2020; 585 :53–57. [PubMed: 32879501]

5. Fan F, et al. Continuous-wave lasing in colloidal quantum dot solids enabled by facet-selective epitaxy. Nature. 2017; doi: 10.1038/nature21424
6. Klimov VI, et al. Optical gain and stimulated emission in nanocrystal quantum dots. Science (80-). 2000; doi: 10.1126/science.290.5490.314
7. Kim YY, et al. Roll-to-roll gravure-printed flexible perovskite solar cells using eco-friendly antisolvent bathing with wide processing window. Nat Commun. 2020; 11 :1–11. [PubMed: 31911652]
8. Xie W, et al. On-Chip Integrated Quantum-Dot–Silicon-Nitride Microdisk Lasers. Adv Mater. 2017; 29
9. Tsiminis G, et al. Nanoimprinted organic semiconductor laser pumped by a light-emitting diode. Adv Mater. 2013; doi: 10.1002/adma.201205096
10. Ujager, FS; Zaidi, SMH; Younis, U. A review of semiconductor lasers for optical communications; 7th Int Symp High-Capacity Opt Networks Enabling Technol HONET 2010; 2010. 107–111.
11. Wang Y, et al. Monolithic quantum-dot distributed feedback laser array on Si. Optica. 2018; 5 :528–533.
12. Rose A, Zhu Z, Madigan CF, Swager TM, Bulović V. Sensitivity gains in chemosensing by lasing action in organic polymers. Nature. 2005; 434 :876–879. [PubMed: 15829959]
13. Vollmer F, Arnold S. Whispering-gallery-mode biosensing: Label-free detection down to single molecules. Nat Methods. 2008; 5 :591–596. [PubMed: 18587317]
14. Karl M, et al. Flexible and ultra-lightweight polymer membrane lasers. Nat Commun. 2018; 9
15. Vannahme C, Klinkhammer S, Lemmer U, Mappes T. Plastic lab-on-a-chip for fluorescence excitation with integrated organic semiconductor lasers. Opt Express. 2011; 19 :8179–86. [PubMed: 21643068]
16. Pradhan S, et al. High-efficiency colloidal quantum dot infrared light-emitting diodes via engineering at the supra-nanocrystalline level. Nat Nanotechnol. 2019; 14 :72–79. [PubMed: 30510279]
17. Kirmani AR, Luther JM, Abolhasani M, Amassian A. Colloidal quantum dot photovoltaics: Current progress and path to gigawatt scale enabled by smart manufacturing. ACS Energy Lett. 2020; 5 :3069–3100.
18. Bi Y, et al. Infrared Solution-Processed Quantum Dot Solar Cells Reaching External Quantum Efficiency of 80% at 1.35 µm and Jsc in Excess of 34 mA cm−2. Adv Mater. 2018; 30
19. Dang C, et al. Red, green and blue lasing enabled by single-exciton gain in colloidal quantum dot films. Nat Nanotechnol. 2012; 7 :335–339. [PubMed: 22543426]
20. Adachi MM, et al. Microsecond-sustained lasing from colloidal quantum dot solids. Nat Commun. 2015; 6 :6–13.
21. Park YS, Bae WK, Baker T, Lim J, Klimov VI. Effect of Auger Recombination on Lasing in Heterostructured Quantum Dots with Engineered Core/Shell Interfaces. Nano Lett. 2015; doi: 10.1021/acs.nanolett.5b02595
22. Roh J, Park YS, Lim J, Klimov VI. Optically pumped colloidal-quantum-dot lasing in LED-like devices with an integrated optical cavity. Nat Commun. 2020; 11 :1–10. [PubMed: 31911652]
23. Özdemir O, Ramiro I, Gupta S, Konstantatos G. High Sensitivity Hybrid PbS CQD-TMDC Photodetectors up to 2 µm. ACS Photonics. 2019; 6 :2381–2386.
24. Wu K, Park YS, Lim J, Klimov VI. Towards zero-threshold optical gain using charged semiconductor quantum dots. Nat Nanotechnol. 2017; doi: 10.1038/NNANO.2017.189
25. Cooney RR, Sewall SL, Sagar DM, Kambhampati P. State-resolved manipulations of optical gain in semiconductor quantum dots: Size universality, gain tailoring, and surface effects. J Chem Phys. 2009; 131
26. Kang I, Wise FW. Electronic structure and optical properties of PbS and PbSe quantum dots. J Opt Soc Am B. 1997; doi: 10.1364/josab.14.001632
27. Schaller RD, Petruska MA, Klimov VI. Tunable Near-Infrared Optical Gain and Amplified Spontaneous Emission Using PbSe Nanocrystals. J Phys Chem B. 2003; 107 :13765–13768.
28. Hoogland S, et al. A solution-processed 1.53 µm quantum dot laser with temperature-invariant emission wavelength. Opt Express. 2006; 14 3273 [PubMed: 19516469]

29. Liao C, et al. Low-threshold near-infrared lasing at room temperature using low-toxicity Ag2Se quantum dots. Nanoscale. 2020; 12 :21879–21884. [PubMed: 33107539]
30. Christodoulou S, et al. Single-Exciton Gain and Stimulated Emission across the Infrared Telecom Band from Robust Heavily Doped PbS Colloidal Quantum Dots. Nano Lett. 2020; 20 :5909–5915. [PubMed: 32662655]
31. Park D, Kim M. Mode analysis of DFB SE lasers. IEEE J Quantum Electron. 1996; 32 :1432–1440.
32. Kogelnik H, Shank CV. Coupled-wave theory of distributed feedback lasers. J Appl Phys. 1972; 43 :2327–2335.
33. Wang Z, et al. Room-temperature InP distributed feedback laser array directly grown on silicon. Nat Photonics. 2015; 9 :837–842.
34. Tian B, et al. Room Temperature O-band DFB Laser Array Directly Grown on (001) Silicon. Nano Lett. 2017; 17 :559–564. [PubMed: 27997215]
35. Kambhampati P. Multiexcitons in semiconductor nanocrystals: A platform for optoelectronics at high carrier concentration. J Phys Chem Lett. 2012; 3 :1182–1190.
36. Cooney RR, Sewall SL, Sagar DM, Kambhampati P. Gain control in semiconductor quantum dots via state-resolved optical pumping. Phys Rev Lett. 2009; 102 :1–4.
37. Moreels I, et al. Size-dependent optical properties of colloidal PbS quantum dots. ACS Nano. 2009; 3 :3023–3030. [PubMed: 19780530]

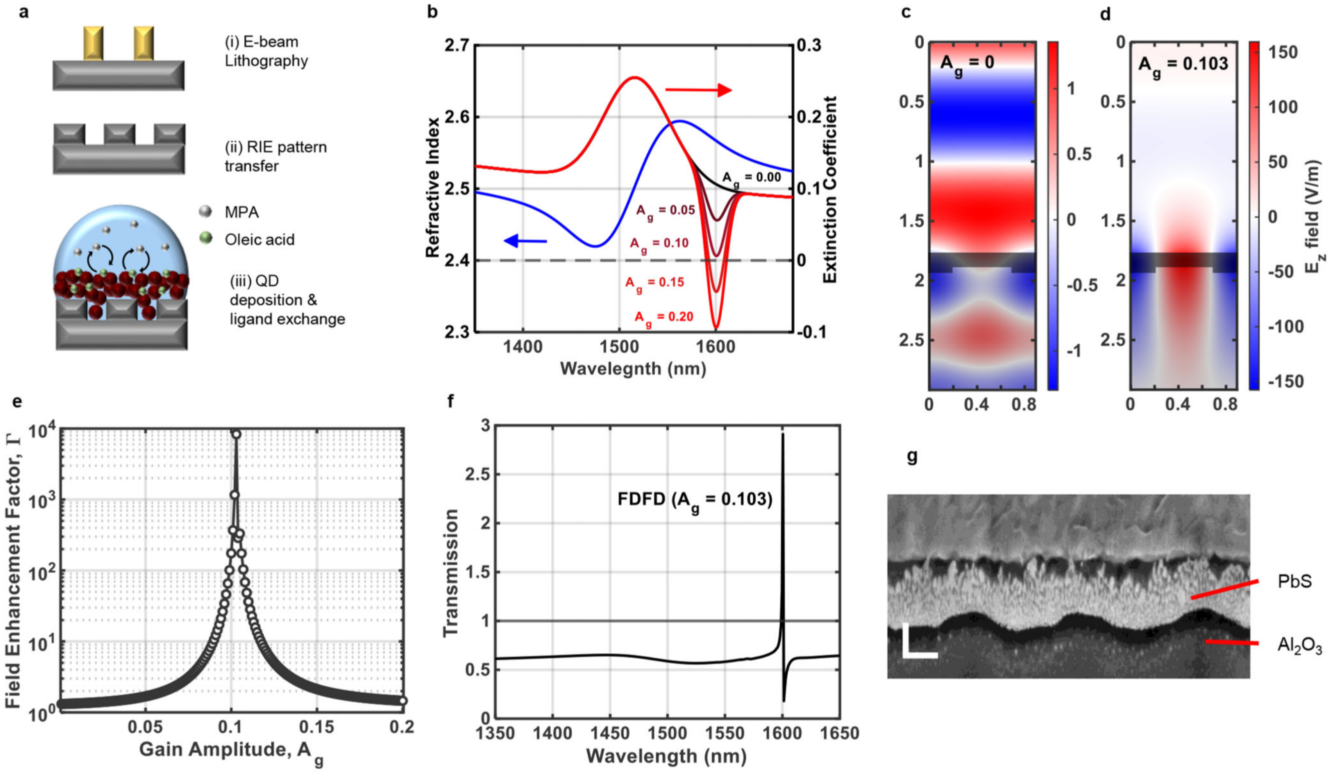

Fig. 1. Device design and fabrication.

(a) Schematic work flow of the fabrication process used for CQD DFB lasers; (i) First e-beam lithography is performed to nanostructure PMMA; (ii) the nanostructure is then transferred to the substrate by reactive ion etching (RIE); (iii) CQDs are deposited on gratings followed by a subsequent ligand exchange. (b) Refractive index (blue) and extinction coefficient (black/red) obtained from ellipsometry and equation (2), with extinction coefficient plotted for different values of A_g as indicated. E_z field 2D plots at 1600 nm for (c) $A_g = 0$ and (d) $A_g = 0.103$. Quantum dots are indicated by the shaded area, and above and below is air and alumina respectively. The grating height is 40 nm, the period is 885 nm, the grating duty cycle is 0.45 (see Supplementary Information section), and the thickness of the quantum dots above gratings is 105 nm. (e) Field enhancement at 1600 nm, calculated using equation 3 (see Methods) plotted as a function of gain amplitude. (f) Simulated transmission spectrum of quantum dot DFB laser for $A_g = 0.103$. (g) Angled SEM image of a FIB cut of a fabricated CQD DFB structures with dimensions matching that of simulations (Supplementary Information II & III) (horizontal scale bar:250 nm and vertical scale bar: 100 nm).

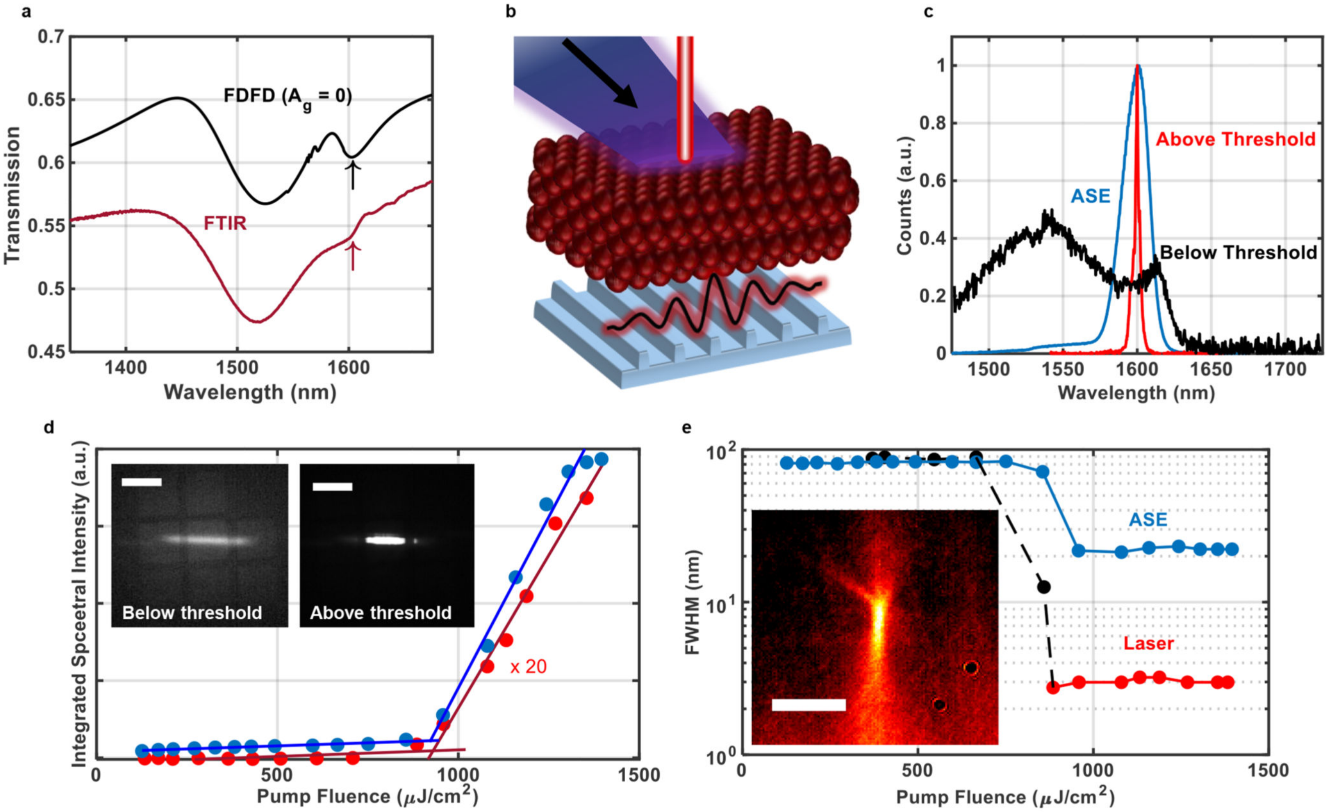

Fig. 2. DFB lasing characterisation.

(a) Transmission spectra simulated using FDFD solver (black) along with that measured via FTIR from the DFB laser sample (red). (b) Diagram showing DFB lasing from CQDs when optically pumped. (c) Spectra collected out-of-plane, perpendicular to the sample surface, below lasing threshold (black) collected using low-resolution settings, and above threshold (red), collected using high resolution settings. The ASE spectra (blue) is also plotted was collected in-plane from the side of the sample. (d) Integrated spectra plotted against pump fluence, used to determine threshold behaviour. Insets show the infrared image of take from the surface of the sample below and above lasing threshold as indicated (scale bar 1 mm). (e) The FWHM of collected lasing and ASE emission spectra plotted as a function of optical pump fluence. Black and red points indicate FWHM obtained from low and high resolution spectra respectively. Inset shows a false-colour infrared beam profile taken 2 cm away from the surface of the sample (scale bar 1 mm).

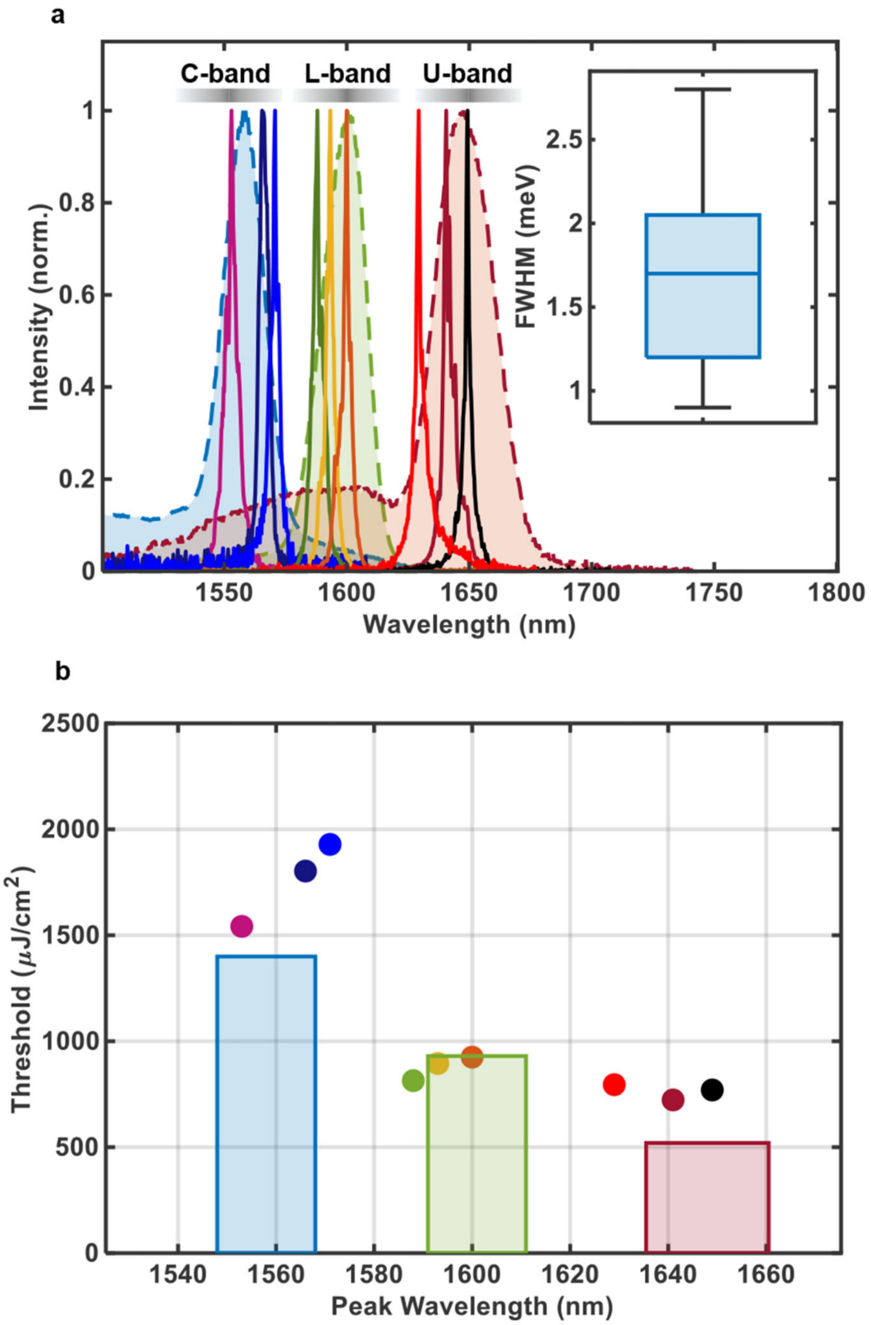

Fig. 3. Infrared lasing tunability.

(a) ASE and lasing spectra from three different quantum dot (5.4 nm (blue), 5.7 nm(green), 6.0 nm(red)) and a varying grating period. The grating periods used of each laser from left to right are: 850 nm, 855 nm, 860 nm, 875 nm, 880 nm, 885 nm, 910 nm, 915 nm and 920 nm. The figure inset shows a box chart of FHWM data as obtained from the 9 different DFB lasers with centre line defined as the median; the box limits as the lower and upper quartiles; and the whiskers as the minimum and maximum values that are not outliers. (b) Points are plotted of the measured lasing threshold against peak wavelength position of each DFB lase, with corresponding colour to that of (a). Bar charts plot the corresponding ASE threshold of each sample, the width of which indicates the FWHM of the ASE spectra.

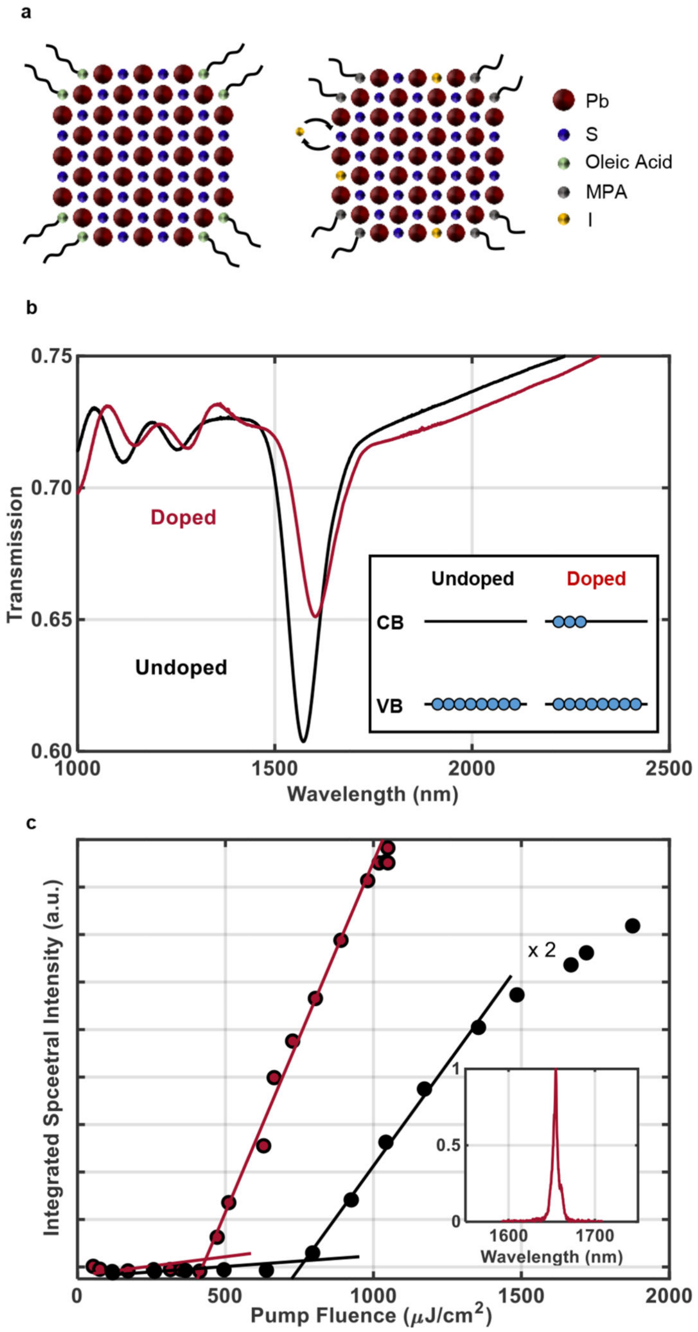

Fig. 4. DFB lasing from n-doped PbS CQDs.

(a) Schematic of PbS quantum dots before (left) and after (right) the ligand exchange procedure. Additionally depicted is the ionic exchange of the S^{2-} and the I^- ions on the (100) surface; doping the quantum dot. (b) Transmission spectra of CQDs before and after the ALD process providing doping demonstrates the absorption quenching due to doping. (c) Optical input/output lasing characteristic of a doped (red) and undoped (black) ~1650 nm CQD DFB lasers. Inset shows the lasing spectra of the doped sample.